RESEARCH ARTICLE

Multifunction Pattern Reconfigurable Slot-Antenna for 5G Sub-6 GHz Small-Cell Base-Station Applications

SAEED HAYDHAH[1], (Student Member, IEEE), **RYAN GOLD**[1], **ZHIYONG DONG**[1],
FABIEN FERRERO[2], (Member, IEEE), **LEONARDO LIZZI**[2], (Senior Member, IEEE),
MOHAMMAD S. SHARAWI[3], (Senior Member, IEEE),
AND AHMED A. KISHK[1], (Life Fellow, IEEE)

[1]Electrical and Computer Engineering Department, Concordia University, Montreal, QC H3G 1S6, Canada
[2]CNRS, LEAT, Université Côte d'Azur, 06410 Sophia Antipolis, France
[3]Electrical Engineering Department, Polytechnique Montréal, Montreal, QC H3T 1J4, Canada

Corresponding author: Saeed Haydhah (saeed.haydhah@concordia.ca)

ABSTRACT A new compact multifunctional pattern reconfigurable 2×2 antenna array at 3.65 GHz with high gain and 16 (Multiple Input Multiple Output) MIMO modes is proposed. The single-element antenna includes 4 U-slots etched on the ground plane, with orthogonal slot orientations for polarization un-correlation, and fed using a reconfigurable feeding network with 4 PIN diodes. Hence, the single-element antenna is a pattern reconfigurable U-slot antenna with four pattern configurations. The average efficiency of 80%, the peak gain of 9.4 dB, and an overlapped -10 dB impedance-bandwidth of 200 MHz at a resonant frequency of 3.65 GHz in the n78 5G band are achieved. The single-element size is 55.5×54 mm^2, $0.66\lambda_0 \times 0.65\lambda_0$. The horizontal and vertical distances between the U-slots in a single-element are 30 mm ($0.36\lambda_0$), and 27 mm ($0.32\lambda_0$), respectively. The 2×2 antenna array of such an element with a 58.5 mm ($0.7\lambda_0$) between the elements occupies a volume of $140 \times 140 \times 21$ mm^3. The 2×2 elements provide 16 reconfigurable U-slots with two modes of operation, Array Mode and Multiple-Input-Multiple-Output (MIMO) Mode. For the MIMO Mode, the antenna has a maximum Envelope Correlation Coefficient (ECC) of 0.1194 between the radiation patterns and a minimum isolation of 20 dB between the four ports. For the array Mode, a 4×4 antenna array has a peak gain of 17 dBi, and a beam-steering range of $-50° \leq \theta \leq 50°$ in the two principle planes. The antenna is suitable for small cell base-station applications.

INDEX TERMS Reconfigurable antennas, small cell, pattern reconfigurable antenna, slot antennas, FR1, Sub-6 GHz.

I. INTRODUCTION

The mobile traffic using 5G technology will increase sharply, with an estimated 5G traffic percentage of 10.6% in 2023 [1]. The typical user data rate will increase by $10 - 100$ times in the 5G technology [2]. Higher data rates are required

The associate editor coordinating the review of this manuscript and approving it for publication was Mahmoud A. Abdalla.

to serve the huge numbers of incoming connections and applications to the network. The 5G technology can provide much higher data rates and the required connections for incoming devices and applications. One of the important technologies in 5G is the Multiple-Input Multiple-Output (MIMO) antenna to enhance the channel capacity without increasing the power consumption. Hence, the user data rates can increase. Furthermore, the use of antennas with high gain

and beam steering capabilities using antenna arrays enhances the received Signal-to-Noise Ratios (SNR) and the channel capacity.

Slot radiators provide a compact antenna design and large antenna arrays for more gains and steering capabilities. The pattern reconfigurability enhances the coverage efficiency of the antenna arrays. Furthermore, pattern reconfigurability allows the antenna to be used for multifunctions (as an array or a MIMO). Pattern reconfigurable slot-based antennas have been proposed in the literature using different approaches [3], [4], [5], [6], [7], and [8]. In [3], an electronically pattern reconfigurable antenna was presented. The antenna was composed of a rectangular patch and a square-ring. It exhibited a radiation efficiency of 70% and a gain of 6.8 dBi. However, the antenna was a single polarization with two low gain patterns and a small bandwidth of 50 MHz around 2 GHz. While in [4], a pattern reconfigurable antenna at 2.4 GHz with a 30 MHz bandwidth was proposed using a patch antenna and four complementary split-ring resonators (CSRRs) to provide 180° or 0° phase shift to achieve different radiation patterns. The antenna size was large, and for a single port, the antenna provided 9 patterns with gains of 5.7 dBi, and 73% radiation efficiency using 8 PIN diodes. In [5], a pattern reconfigurable antenna at 2.4 GHz with 4 L-shaped slots was presented. The antenna exhibited 10 patterns using 4 PIN diodes, with a single port and a compact size. However, the antenna only had bandwidth of 100 MHz, small gains of 2 dBi, a single linear polarization, Envelop Correlation Coefficient (ECC) values that reached 0.4 in some cases, and a wide Half Power Beam Widths (HPBWs) in the elevation plane. The work in [6] proposed a wide-band pattern reconfigurable tapered-slot antenna at 2 GHz, obtained using 4 PIN diodes, enabling 4 patterns with a gain of 6.4 dBi and a radiation efficiency of 70%. The PIN diodes were installed across the slot-lines, thus degrading the radiation performance of the antenna. In [7], a linearly polarized bulky pattern reconfigurable patch-slot-ring antenna at 2.4 GHz was presented. The diodes across the slot were used to redirect the current paths on the patch and the rectangular ring. The antenna achieved a bandwidth of 2 GHz, with a gain of 3 dBi. However, four radiation patterns were achieved using 6 PIN diodes. In [8], a pattern reconfigurable cross-shape slot antenna at 5 GHz was obtained with two parasitic slots as a director or a reflector using two PIN diodes to reconfigure their lengths. The antenna had three broadside radiation patterns due to a magnetic conductor located a quarter wavelength below the slot. The antenna bandwidth was 1.7 GHz and a gain of 6 dBi. However, the antenna size was large, although the resonant frequency was relatively high.

The literature has many MIMO designs, those in [9], [10], [11], [12], [13], [14], [15], [16], [17], [18], [19], and [20]. The design in [9] was a MIMO antenna for the WLAN 2.4/5.2/5.8 GHz bands, using three dual-loop antennas, which achieved a bandwidth of 200 MHz and a radiation gain of 6.5 dBi. However, it was only a MIMO antenna with an isolation of 15 dB. The design in [10]

was a six-port MIMO antenna for WLAN 5 GHz band small-cell base-stations, which achieved high isolation of 44 dB between the six ports with dual linear polarization capability. However, the structure was bulky, although the resonant frequency was relatively high. The ECCs in [9] and [10] were calculated using the S-parameter equation. The operation bandwidth in [10] was 1.16 GHz, which is wide considering its high resonant frequency, but the 6.5 dBi gain was low considering the large size of the antenna. The design in [11] was a triple-band MIMO antenna for small-cell base-stations with large size, achieving radiation gain of around 8 dBi with a maximum bandwidth of 800 MHz in the 5.2 GHz band, and the maximum ECCs were around 0.1. In [12], [13], [14], [15], [16], [17], [18], [19], and [20], pattern reconfigurable MIMO antennas were presented, which can be compared with the proposed 2 × 2 antenna array in this article. In [12], a WiFi pattern reconfigurable MIMO antenna with three pattern states at 2.45 GHz based on the excitation of 3 different characteristic modes was presented. It has achieved a bandwidth of 200 MHz, a high ECC of 0.5, low radiation efficiency of 60%, and only 3 MIMO states. The work in [13] demonstrated a pattern and polarization reconfigurable Multi-User MIMO antenna using a parasitic tuning technique to obtain four patterns and three polarizations. However, the design was very complex, using lots of PIN diodes to achieve reconfigurability. The proposed work in [14] presented a pattern and frequency reconfigurable MIMO array of four elements at 3.6 and 5.5 GHz, with four pattern states achieved by orthogonal orientations of the elements, and frequency reconfigurability was achieved by filling a cavity with water or with air. The design achieved bandwidths of 200 and 775 MHz at 3.6 and 5.5 GHz, respectively, a maximum ECC of 0.016, a low gain of 4.6 dBi, and a radiation efficiency of 80%. It can also be observed that the design was very complex as it was required to fill a cavity with water to reconfigure the resonant frequency. Another design was presented in [15], showing a pattern reconfigurable cavity-backed metasurface 2 × 2 MIMO antenna at 5.9 GHz, with a pattern reconfigurability that was achieved by electrically tuning the unit cells above the cavity antennas. The design size was large and very complex, using around 100 PIN diodes. The work in [16] showed a pattern reconfigurable dual-antenna array using a monopole and a Planar Inverted F (PIFA) antennas at 2.65 GHz with two pattern states. The design achieved a narrow bandwidth of 96 MHz, a maximum ECC of 0.05, a low gain of 3 dBi, a low port isolation of 15 dB, and a medium complexity. The demonstrated design in [17] was a pattern reconfigurable MIMO antenna at 2.45 GHz with three pattern states using a monopole and two sets of parasitic strips that can be electrically reconfigured to work as a director or a reflector. The design achieved a low gain of 4.7 dBi, low isolation of 16.5 dB, and a low number of 9 MIMO states. A pattern reconfigurable MIMO antenna with two elements was proposed in [18] at 2.45 GHz using a Coplanar Waveguide feed line and two C-shaped metallic radiators that

can be reconfigured electrically. The work in [19] presented a pattern reconfigurable planar array antenna based on digital coding characterization. However, the antenna size was very large, with a very narrow bandwidth of 50 MHz, and highly complex using 64 PIN diodes.

This work proposes a new compact sub-6 GHz dual-polarized pattern reconfigurable slot-based 2×2 antenna array. The antenna resonant frequency is 3.65 GHz in the n78 5G band. The 2×2 antenna has two functional modes: the MIMO Mode and the Array Mode. The novelty is considered due to the single-element compactness of a size of 54×55.5 mm^2 and high performance. In addition, the single-element antenna enables 4 different radiation patterns with high directivities and very low ECC using only 4 PIN diodes and one feeding port (the maximum ECC between the patterns of a single-element is 0.18 within the bandwidth). Furthermore, the antenna exhibits a bandwidth of 200 MHz, a minimum peak gain of 9 dBi, and minimum radiation efficiency of 80%. Also, the single-element antenna achieves two reconfigurable linear polarizations. In addition, the antenna array has multifunctional operation as 2×2 elements MIMO with 16 different MIMO states to enhance the channel capacity with very low ECCs (lower than 0.1194), and as an array to enhance the antenna gain and beam steering capability within a wide view range. The rest of the paper consists of four sections. Section II presents the antenna geometry and theory. Section III presents the numerical and experimental results of the single-element antenna. Section IV shows the numerical and experimental results of the 2×2 and 4×4 antenna array. Section V discusses the obtained results, compares them with previous proposed small-cell base-station antennas and pattern reconfigurable MIMO antennas, and concludes the paper.

II. ANTENNA GEOMETRY AND THEORY

A. SINGLE-ELEMENT ANTENNA GEOMETRY

Fig. 1 shows the proposed single-element pattern reconfigurable antenna. A reflector is placed below the single-element antenna at a distance of quarter-wavelength at 3.65 GHz. It can be seen from Fig. 1 that the single-element antenna is composed of a single FR-4 substrate with a dielectric constant of $\epsilon_r = 4.4$, a loss tangent of $tan\delta = 0.02$, and a thickness of h = 0.8 mm. FR-4 material is chosen so that a low-cost antenna is achieved. The bottom face of the antenna includes the ground plane etched by 4 U-shaped slots. The ground plane is brown in Fig. 1, the FR-4 substrate exposed surface is light-blue, and the feeding network is printed on the top face presented in black color. The FR-4 material above the U-shaped slots is removed to enhance the antenna radiation efficiency. The 4 U-shaped slots are rotated by 90° to achieve two orthogonal linear polarizations and to un-correlate between the four radiation patterns. The U-slots are half-wavelength slots, and the horizontal and vertical separation between the U-slots is 0.36 λ_0 and 0.32 λ_0, respectively. The top face of the antenna includes the reconfigurable feeding network and the biasing circuits. The
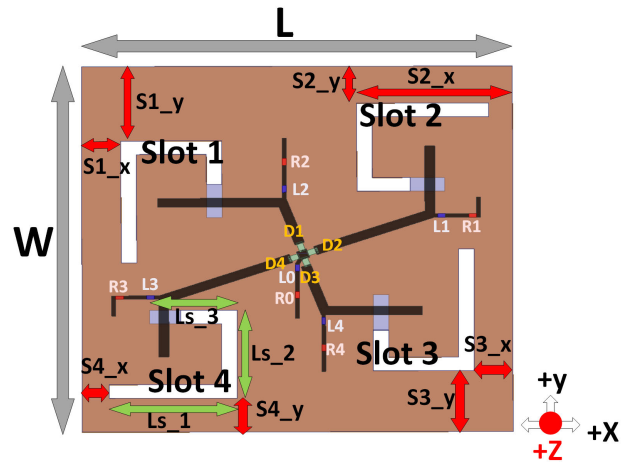

FIGURE 1. Geometry of a single-element antenna. The black feeding microstrip line network is on top, the ground plane at the bottom is brown, light blue is the exposed dielectric substrate, and white is air (removed dielectric).
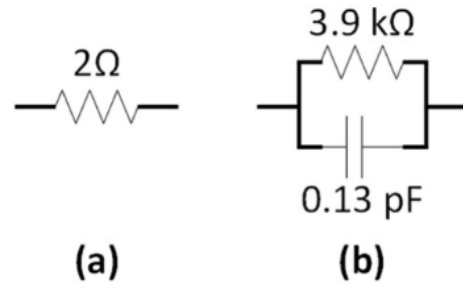

FIGURE 2. Diode's equivalent circuit models used in the full-wave simulation. (a) PIN diode is 'ON' and (b) PIN diode is 'OFF.'

single-element antenna is fed by a single coaxial port at its center. The inner conductor of the coaxial cable is connected to the center feeding pad, as shown in Fig. 1. Four PIN diodes are used to switch between the four transmission lines feeding (exciting) the U-shaped slots. The single-element antenna achieves four uncorrelated unidirectional radiation patterns at 3.65 GHz that are reconfigured electrically using the four PIN diodes (Infineon BAR64-02 V PIN diodes, 10 mA flows through the PIN diode when it is ON, with a power consumption of 10 mW). The PIN diodes are shown in green in Fig. 1. The equivalent circuit models for the 'ON' and 'OFF' PIN diodes are shown in Fig. 2. The size of this single-element antenna is 55.5×54 mm^2, i.e., $0.66 \times 0.65 \lambda_0^2$ at 3.65 GHz. The biasing circuit for a PIN diode includes R.F. chokes of 30 nH (L0 $-$ L4 in blue in Fig. 1) and 220 Ω resistors (R0 $-$ R4 in red in Fig. 1), allowing a current of 10 mA to flow through the 'ON' diode. The dimensions of the parameters shown in Fig. 1 are given in Table 1.

The microstrip line's stub length and slot crossing position are used to optimize the antenna input impedance. The slot length is used to change the antenna resonant frequency, while the slot width is optimized to tune the resonant frequency and improve the matching bandwidth. The 4 U-slot

Parameter	Length (mm)	Parameter	Length (mm)
L	55.5	W	54
Slot Width	2	Ls_1	16.5
Ls_2	13	Ls_3	11.3
$S1_x$	5.06	$S1_y$	11
$S2_x$	20.06	$S2_y$	5.46
$S3_x$	5	$S3_y$	9
$S4_x$	3.5	$S4_y$	5
Reflector h	20.3	T.L Width	1.3
Substrate h	0.8	U-Slot Length	37

positions are chosen to reduce the mutual coupling between the slots. The feeding network is reconfigurable with four PIN diodes and four transmission lines. The feeding network is designed to enable four different pattern configurations. First, the rectangular pad dimensions are optimized for input impedance matching; the four PIN diodes are installed, and then the four 50Ω microstrip transmission lines are printed to feed the U-slots. The PIN diodes' positions are chosen, as shown in Fig. 1, to achieve good input impedance matching. On the other hand, the FR-4 material above the U-slots are removed to improve the radiation efficiency of the slot radiators. The FR-4 material is lossy, and as a result, it reduces the radiation efficiency of the radiating U-slot. Therefore, the radiation efficiency increases sharply when the FR-4 material is removed above the U-slot, where the electric field is high. However, the resonant electrical length of the slot is increased because the effective permittivity is reduced by removing the FR-4 dielectric. The antenna is fabricated using the commercially available process without extra cost.

B. ANTENNA DESIGN THEORY

The U-Slot shape is chosen to enhance the operating bandwidth, reduce slot area, and achieve pattern reconfigurability for the single-element antenna. The slot length is half-wavelength and fed by a microstrip line. The microstrip line position and stub length are optimized to enhance the matching bandwidth. The orthogonal orientations of the U-slots with respect to each other lower ECCs and provide better pattern reconfigurability. A sketch of the magnetic current distribution when Slot 1 is excited (only D1 is ON), is shown in Fig. 3. The joint distribution of the magnetic currents $M1$, $M2$ and $M3$ is a cosine function, because the electric field maximum is at the middle of $M2$'s slot, then the electric field decreases gradually until field nulls are achieved at the bottom ends of $M1$'s and $M3$'s slots. The electric field in $M1$'s slot is in the opposite vector direction and approximately close in magnitude to the electric field in $M3$'s slot. Therefore, it is reasonable to assume that the currents $M1$ and $M3$ partially cancel each other. Thus, they approximately do not contribute to broadside radiation. Thus, $M2$ is approximately the only current providing broadside radiation. This assumption is reasonable allowing us to

reach an approximate theoretical explanation for the antenna radiation, which is very close to the lengthy exact approach. The radiation pattern, as a result, is bidirectional above and below the ground plane. Thus, a reflector is added below the antenna making the radiation pattern uni-directional. In addition, the magnetic current $M4$ along Slot 4 works as a director. Thus, the radiation pattern is tilted toward the $-y$ direction. The same current distributions with different orientations take place when Slot 2, Slot 3, or Slot 4 is excited. Therefore, the four U-slots produce four uncorrelated radiation patterns.

When Slot 1 is excited, assuming that the electric field on the slot aperture is uniform and directed to y-direction along the part of the slot where $M2$ resides. The slot aperture electric field can be written as [21].

$$\vec{E}_a = E_o \vec{a}_y \qquad (1)$$

So, the equivalent magnetic current $M2$, can be written as [21].

$$\vec{M}_2 = -2\vec{n} \times \vec{E}_a \qquad (2)$$

Therefore, the far-fields of Slot 1 could be written as [21].

$$E_r = H_r = 0 \qquad (3)$$

$$E_\theta = C sin\phi \frac{sinX}{X} \frac{sinY}{Y} \qquad (4)$$

$$E_\phi = C cos\theta cos\phi \frac{sinX}{X} \frac{sinY}{Y} \qquad (5)$$

$$H_\theta = -\frac{E_\phi}{\eta} \qquad (6)$$

$$H_\phi = \frac{E_\theta}{\eta} \qquad (7)$$

where X, Y and C are [21].

$$X = \frac{ka}{2} sin\theta cos\phi \qquad (8)$$

$$Y = \frac{ka}{2} sin\theta sin\phi \qquad (9)$$

$$C = j \frac{abkE_o e^{-jkr}}{2\pi r} \qquad (10)$$

where a and b are the length and width of the $M2$ slot, and k is the propagation constant in free space. The far fields in E-plane ($\phi = 90^o$) can be written as

$$E_r = E_\phi = 0 \qquad (11)$$

$$E_\theta = C \frac{sin(\frac{kb}{2} sin\theta)}{\frac{kb}{2} sin\theta} \qquad (12)$$

and the H-plane ($\phi = 0$) far fields are

$$E_r = E_\theta = 0 \qquad (13)$$

$$E_\phi = C cos\theta \frac{sin(\frac{kb}{2} sin\theta)}{\frac{kb}{2} sin\theta} \qquad (14)$$

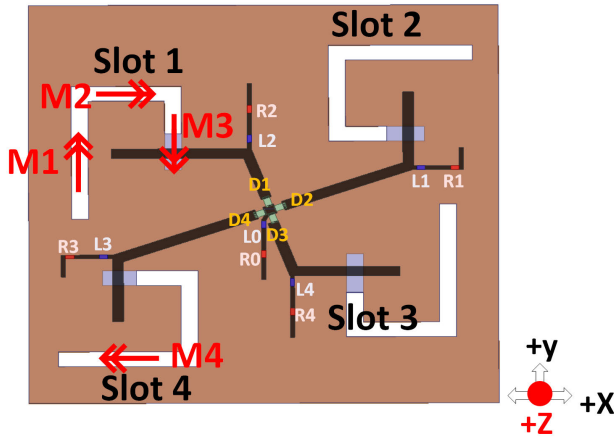Slot 1 is y-polarized, but the cross-polarization is high because the magnetic currents $M1$ and $M3$ contributions do

FIGURE 3. Magnetic current distribution sketch on a single-element antenna when D1 is ON, and D2−D4 are OFF.

FIGURE 4. Simulated electric surface current for the four configurations of the single-element antenna.

not cancel each other completely since the lengths of the two side slots are not equal. The radiation pattern is bidirectional. Hence, a reflector is added below the single-element antenna by quarter-wavelength and image theory is used to predict the radiation pattern of Slot 1 as a linear array of two in-phase magnetic current elements along the Z-axis separated by half-wavelength. The normalized array factor of the linear array is written in Eq. (15).

$$(A.F.)_n = cos\left[\frac{1}{2}(kdcos\theta + \beta)\right] \tag{15}$$

where $k = 2\pi/\lambda$, $d = \lambda/2$ and $\beta = 0$, and Eq. (15) can be simplified to Eq. (16).

$$(A.F.)_n = cos\left[\frac{1}{2}(\pi cos\theta)\right] \tag{16}$$

Hence, two nulls are generated at $\theta = 0^o$ and $\theta = 180^o$, and the main lobe peak occurs at $\theta = 90^o$. Therefore, the array factor supports the tilt of the radiation pattern of Slot 1 when the magnetic current $M4$ of Slot 4 acts as a director to Slot 1. Furthermore, it can be seen from Fig. 4, showing the simulated surface electric currents for each slot configuration, that the proposed single-element antenna follows the Yagi-Uda radiation concept. It can be seen from Fig. 4 that when Slot 1 Configuration is excited, the current at the reflector side is longer than the dominant radiating electric current around the top part of Slot 1, making it work as another reflector, while the electric current at the director side is shorter than the dominant radiating current, making it work as a director.

The same theoretical approach is used to explain the radiation patterns generated from Slot 2, Slot 3, and Slot 4. Hence, the proposed single-element antenna achieves four uncorrelated radiation patterns and two orthogonal polarizations.

C. RECONFIGURATION MECHANISM

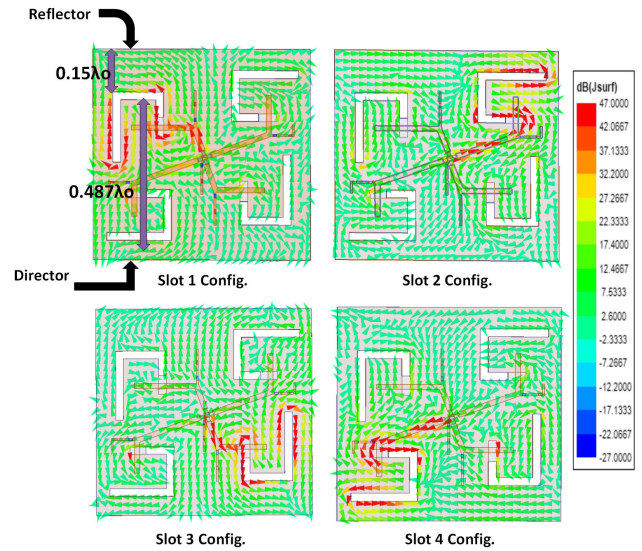The four radiation patterns of the proposed single-element antenna are reconfigured using four PIN diodes (D1−D4),
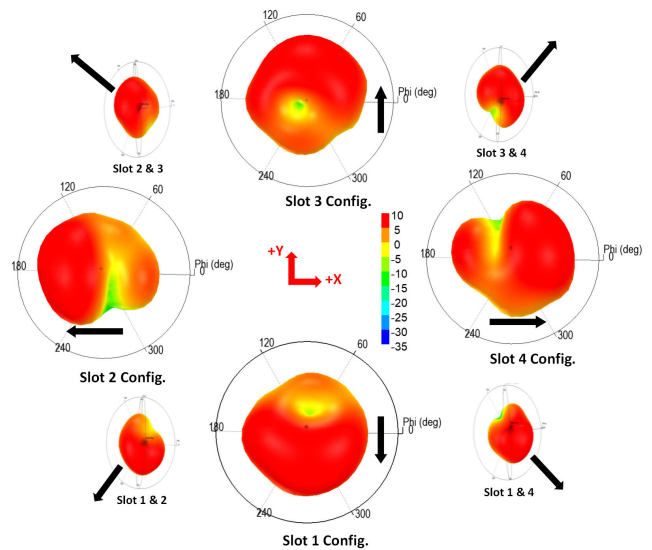

FIGURE 5. Simulated 3D radiation patterns for the pattern configurations of the single-element antenna.

TABLE 2. Pattern Configurations of a Single-Element Antenna.

Config.	Tilt Direction	Polarization	'ON' Diode	'OFF' Diodes
Slot 1	−y	along y	D1	D2, D3, D4
Slot 2	−x	along x	D2	D1, D3, D4
Slot 3	+y	along y	D3	D1, D2, D4
Slot 4	+x	along x	D4	D1, D2, D3

as shown in Fig. 1. When one diode is ON, the radiation pattern is unidirectional to broadside and tilted to ± x or ± y. The pattern configurations have linear polarizations along the x− or y−direction. The pattern configurations of the
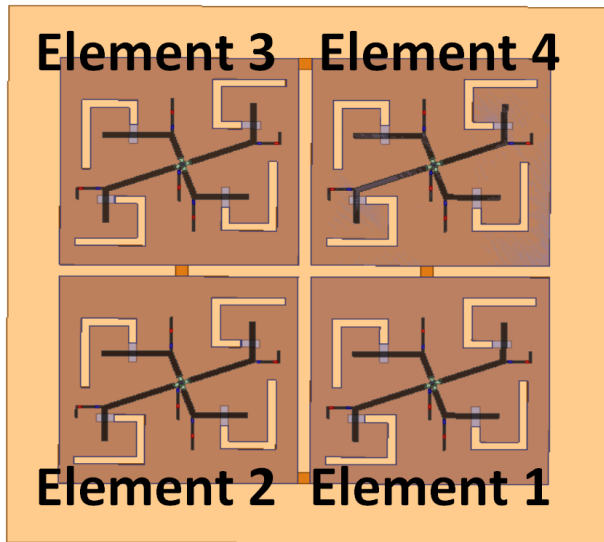
FIGURE 6. 2 × 2 antenna array geometry backed by a reflector at 21 mm from the array bottom.

proposed single-element antenna are summarized in Table 2 and Fig. 5. The four radiation patterns are uncorrelated and suitable for MIMO antenna applications. It can also be seen from Fig. 5 that when two diodes are ON simultaneously, then four more different radiation patterns can be achieved. The simulated and measured results are discussed in the next section.

D. 2 × 2 ANTENNA ARRAY LAYOUT
The single-element antenna is optimized for a 2 × 2 array and MIMO antenna applications, as shown in Fig. 6. Each antenna element in Fig. 6 is fed by a single feeding port. Therefore, 2 × 2 elements have 4 feeding ports and a common ground plane that connects all elements at four positions, as shown in Fig. 6. The locations of ground plane connection points are optimized to maximize the isolation between the four feeding ports. The elements are at 58.5 mm (0.7 λ_0) from each other, making a 3 mm gap on the ground plane. The reflector backing the 2 × 2 elements is 140 × 140 mm^2.

The 2 × 2 elements have two functional modes. Mode I is the Array Mode, where the corresponding diodes on each element have the same activation state simultaneously. So, if the mutual coupling is ignored, each element has the same radiation pattern with enhanced antenna gain. Also, it would be possible to have steering capabilities by varying the elements' phase distributions. It can be observed that when D1 is ON on the four elements, the beam steers to the −y direction. The radiation performance is also improved to ± x or +y when the corresponding diodes are ON. Mode II is the MIMO Mode, and a different pattern is obtained for each element, i.e., different diodes (D1−D4) are activated at the same time for each element of the array. In this case, the MIMO antenna is achieved because the four radiation patterns from the four elements are uncorrelated with ECCs

below 0.1194 and significant isolation between the elements. The simulated and measured results of the two functional modes are discussed in the following sections.

III. NUMERICAL AND EXPERIMENTAL RESULTS OF SINGLE-ELEMENT ANTENNA
The antenna is fabricated, and Fig. 7 shows the photos of the fabricated antennas. The antenna is simulated using Ansys High Frequency Simulation Software (HFSS) version 2020. The S-parameters are measured using the network analyzer PNA - N5227A. The far-field radiation patterns are measured in the Anechoic Chamber. The simulated and measured $|S_{11}|$ of a single-element are in good agreement, as shown in Fig. 8. The results show that the resonant frequencies are around 3.65 GHz and −10 dB impedance bandwidths are 200, 170, 200, and 200 MHz for Slot 1, Slot 2, Slot 3, and Slot 4, respectively. The −10 dB common bandwidth can be taken as 170 MHz. The slight discrepancy between measured and simulated $|S_{11}|$ is due to the presence of the coaxial cable, and the inaccurate values of the inductors, resistors, and PIN diodes. The simulated peak gains of the four pattern configurations are 8.4, 10, 10, and 9 dBi for Slot 1, Slot 2, Slot 3 and Slot 4, respectively, as shown in Fig. 9. The corresponding radiation efficiencies are shown in Fig. 9. The simulated efficiencies are 80.5%, 78.3%, 82.5%, and 78.2%, respectively. On the other hand, the corresponding measured peak gains are 6.5, 8.5, 8, and 7 dBi, as shown in Fig. 10. The 2 or 1.5 dB difference between the measured and simulated gains is due to the coaxial connectors and the coaxial cable (2 to 3 connectors are used because the dimensions of the antenna port connector are different from the dimensions of the coaxial cable connector). It is also important to use the in-between connectors such that it is easier to connect the coaxial cable to the antenna feeding port.

Fig. 10 shows the simulated and measured 2D radiation patterns for four pattern configuration states. The measured and simulated results are in good agreement. Figs. 10((a) and (e)) show that the pattern reconfigurability occurs along the Y-Z plane for Slot 1 and Slot 3 with a y-polarization. Figs. 10((d) and (h)) show that the pattern reconfigurability occurs along the X-Z plane for Slot 2 and Slot 4 with an x−polarization. The radiation patterns are unidirectional, with a minimum simulated Front-to-Back Ratio (FTBR) of 19 dB. Regarding Figs. 10((a), (d), (e) and (h)), the simulated and measured results of the radiation patterns of the single-element antenna are summarized in Table 3. The pattern reconfigurability is achieved along the X-Z and Y-Z planes. The measured peak direction is precisely the same as from the simulation. The measured Side-Lobe Levels (SLLs) are lower than the simulated SLLs, indicating that the coupling between the slots is lower than the simulated ones.

Generally, the measured and simulated results of the pattern reconfigurable single-element are in reasonable agreement. The discrepancy between measured and simulated
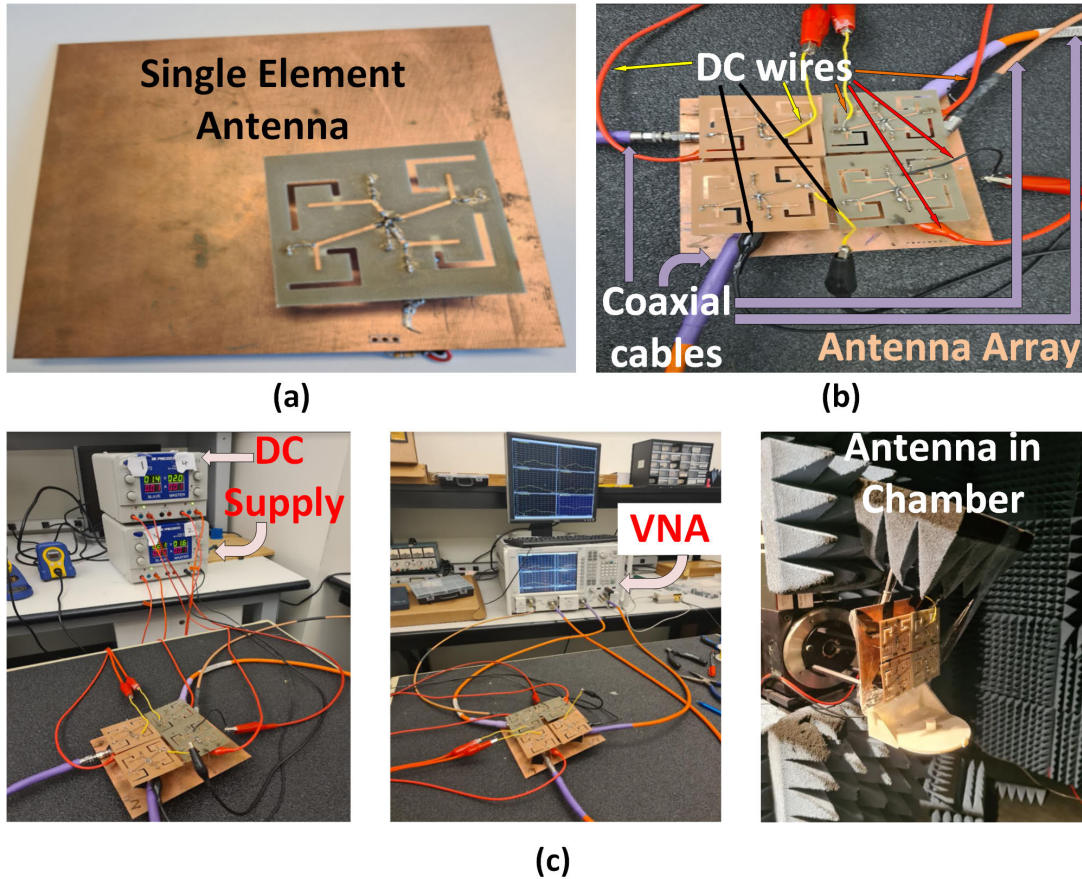
FIGURE 7. Photos of the proposed antenna. (a) Pattern reconfigurable single-element. (b) 2 × 2 antenna array, and (c) 2 × 2 antenna array under test.
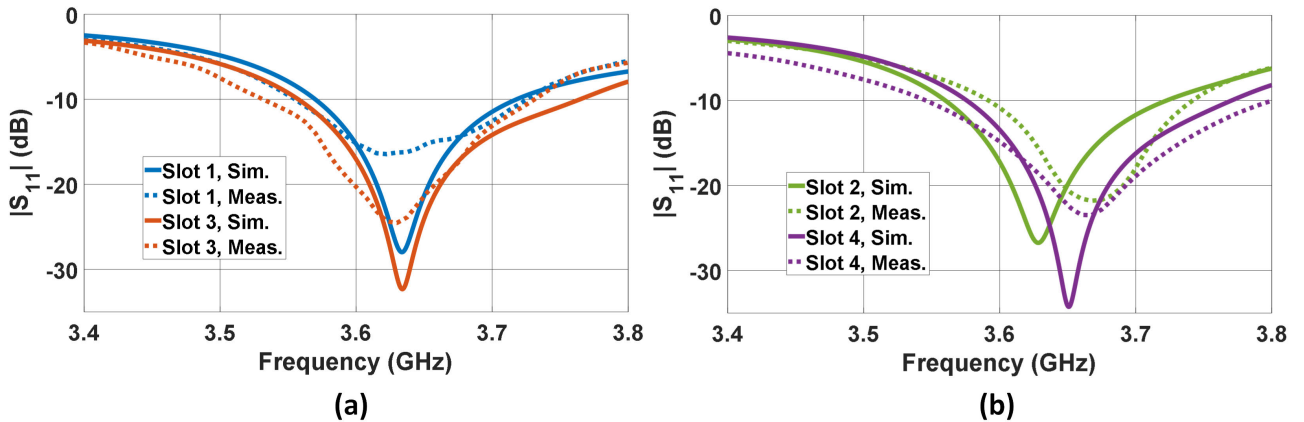

FIGURE 8. Simulated and measured $|S_{11}|$ for the pattern reconfigurable single-element antenna. (a) Slot 1 Configuration and Slot 3 Configuration, and (b) Slot 2 Configuration and Slot 4 Configuration.

radiation patterns is due to the inevitable cable radiations, misalignment of the reflector, and tolerances of the used PIN diodes, inductors and resistors. In addition, when the coaxial cable is connected to the antenna, it could mis-orient it vertically or horizontally from its simulated position during the measurements. Finally, the other sources of errors are cable radiations and D.C wires radiations.

The measurements were done to reduce these errors as much as possible. It is also worth mentioning that the measured radiation patterns are only on the antenna's front side due to the mounting structure, which can only rotate from -90° to $+90^o$ in the azimuthal plane. In addition, as the antenna is active, it needs D.C biasing during the measurements, and it is difficult to flip the antenna manually
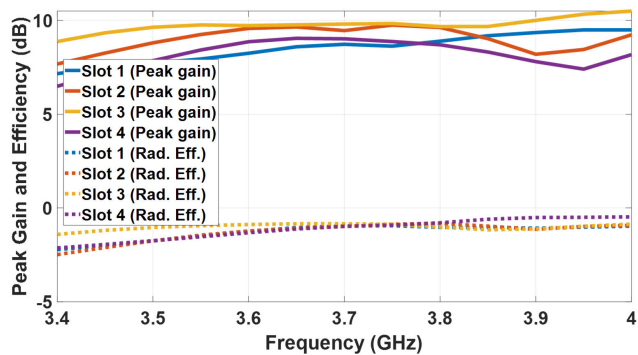
FIGURE 9. Simulated peak gains and radiation efficiencies of the pattern reconfigurable single-element antenna.

TABLE 3. Simulated and Measured Radiation Patterns of a Single-Element Antenna Along the Reconfigurability Plane.

Config.	Sim. θ_{max}	Meas. θ_{max}	Sim. HPBW	Meas. HPBW
Slot 1	−30° (Y-Z)	−30°	45°	47°
Slot 2	−30° (X-Z)	−30°	45°	40°
Slot 3	30° (Y-Z)	30°	40°	42°
Slot 4	30° (X-Z)	30°	45°	45°

and connect it to the rotating arm during the radiation pattern measurements.

IV. NUMERICAL AND EXPERIMENTAL RESULTS OF THE 2 × 2 ANTENNA ARRAY

The 2 × 2 antenna has 16 slots and 16 PIN diodes, as shown in Fig. 6 and the photos of the fabricated array are shown in Fig. 7. The radiation pattern for each slot in the 2 × 2 antenna is shown in Fig. 11. Table 4 summarizes the results of the radiation patterns, when a single slot in the array radiates, which are shown in Fig. 11. It can be seen from Table 4 and Fig. 11 that the simulated and the measured results are in a reasonable agreement. The sources of errors stated before are the same, although some absorbers are used to cover the cable during the measurements. The slots' peak gain in the single-element is different from that in the 2×2 antenna due to ground plane deformation because of the gaps at the contact points between the ground planes.

In general, it can be seen from Fig. 11 that the measured radiation patterns show higher directivity and lower SLLs. The SLL of the measured pattern is higher than the simulated pattern in one case shown in Fig. 11(a2) when Slot 1 in Element 2 is activated, showing that the current distribution of the slots is slightly different from the simulated one. In addition, the measured radiation nulls could differ from the simulated nulls due to the inevitable misalignment of the element antenna above the reflector.

A. ARRAY MODE RESULTS

In the Array Mode, the same diodes (D1−D4) are ON on the four elements, e.g., D1 is ON on all elements, and D2−D4 are OFF on all elements. Therefore, the gain increases, thanks to the array factor of the 2 × 2 array. The achieved gains for

TABLE 4. Simulated and Measured Results of Radiation Patterns of Each Slot in a 2 × 2 array Along the Reconfigurability Plane, with Reference to Fig. 11.

Configuration	Sim. θ_{max}	Meas. θ_{max}	Meas. Gain (dB)	HPBW
Element1, Slot 1	−25° (Y-Z)	−25°	5.5	40°
Element1, Slot 2	−20° (X-Z)	−30°	7	48°
Element1, Slot 3	40° (Y-Z)	40°	6.5	30°
Element1, Slot 4	25° (X-Z)	30°	7	30°
Element2, Slot 1	−23° (Y-Z)	−22°	7	30°
Element2, Slot 2	−20° (X-Z)	−23°	6.7	40°
Element2, Slot 3	30° (Y-Z)	27°	6.7	40°
Element2, Slot 4	30° (X-Z)	20°	6.5	62°
Element3, Slot 1	−30° (Y-Z)	−15°	7	54°
Element3, Slot 2	−22° (X-Z)	−23°	7	38°
Element3, Slot 3	30° (Y-Z)	45°	7	40°
Element3, Slot 4	34° (X-Z)	30°	6.5	52°
Element4, Slot 1	−35° (Y-Z)	−23°	7	54°
Element4, Slot 2	−35° (X-Z)	−17°	6.5	33°
Element4, Slot 3	30° (Y-Z)	33°	6.5	79°
Element4, Slot 4	30° (X-Z)	25°	6.4	51°

the four pattern configurations for the 2 × 2 antenna array are around 12.5 dBi. The antenna array has four elements, so the array gain should be about 6 dB higher than the single-element gain. However, the achieved gain is less than expected due to the mutual coupling and the losses of the feeding network.

The radiation pattern of the single slot is known as discussed in Section II. Now, the array factor of the proposed 2 × 2 planar array can be written as shown in Eq. (17), as presented in [21].

$$A.F._n(\theta, \phi) = \left[\frac{1}{M} \frac{sin(\frac{M}{2}\Phi_x)}{sin(\frac{\Phi_x}{2})} \right] \left[\frac{1}{N} \frac{sin(\frac{N}{2}\Phi_y)}{sin(\frac{\Phi_y}{2})} \right] \quad (17)$$

where

$$\Phi_x = kd_x sin\theta cos\phi + \beta_x \quad (18)$$

$$\Phi_y = kd_y sin\theta sin\phi + \beta_y \quad (19)$$

where $d_x = 58.5$ mm $= 0.7\lambda_o$, and $d_y = 57$ mm $= 0.68\lambda_o$. Taking $M = 2$ and $N = 2$, we can simplify the array factor in the E- and H-plane as shown in Eq. (20), and Eq. (21), respectively.

$$A.F._n(\theta, \phi = 90^o) = \frac{1}{2} \frac{sin(1.36\pi sin\theta + \beta_y)}{sin(0.68\pi sin\theta + \beta_y)} \quad (20)$$

$$A.F._n(\theta, \phi = 0^o) = \frac{1}{2} \frac{sin(1.4\pi sin\theta + \beta_x)}{sin(0.7\pi sin\theta + \beta_x)} \quad (21)$$

where it can be seen that the radiation pattern due to the planar array is controlled by β_y in the E-plane and by β_x in the H-plane, consequently, and the final radiation pattern from the planar array follows the total electric field shown in Eq. (22).

$$E_{total} = E(single\ slot(M_2)) \times A.F.(imaged\ current) \\ \times A.F.(planar\ array) \quad (22)$$

where $E(single\ slot(M_2))$ is the electric field due to the single slot, $A.F.(imaged\ current)$ is the array factor due to the magnetic current M_2, and its image resulted because of the

(a) Slot 1. E_co-pol on the Y-Z Plane.

(b) Slot 1. E_co-pol on the X-Z Plane.

(c) Slot 2. E_co-pol on the Y-Z Plane.

(d) Slot 2. E_co-pol on the X-Z Plane.

(e)Slot 3. E_co-pol on the Y-Z plane.

(f) Slot 3. E_co-pol on the X-Z plane.

(g) Slot 4. E_co-pol on the Y-Z plane.

(h) Slot 4. E_co-pol on the X-Z plane.

— Simulated Radiation Pattern

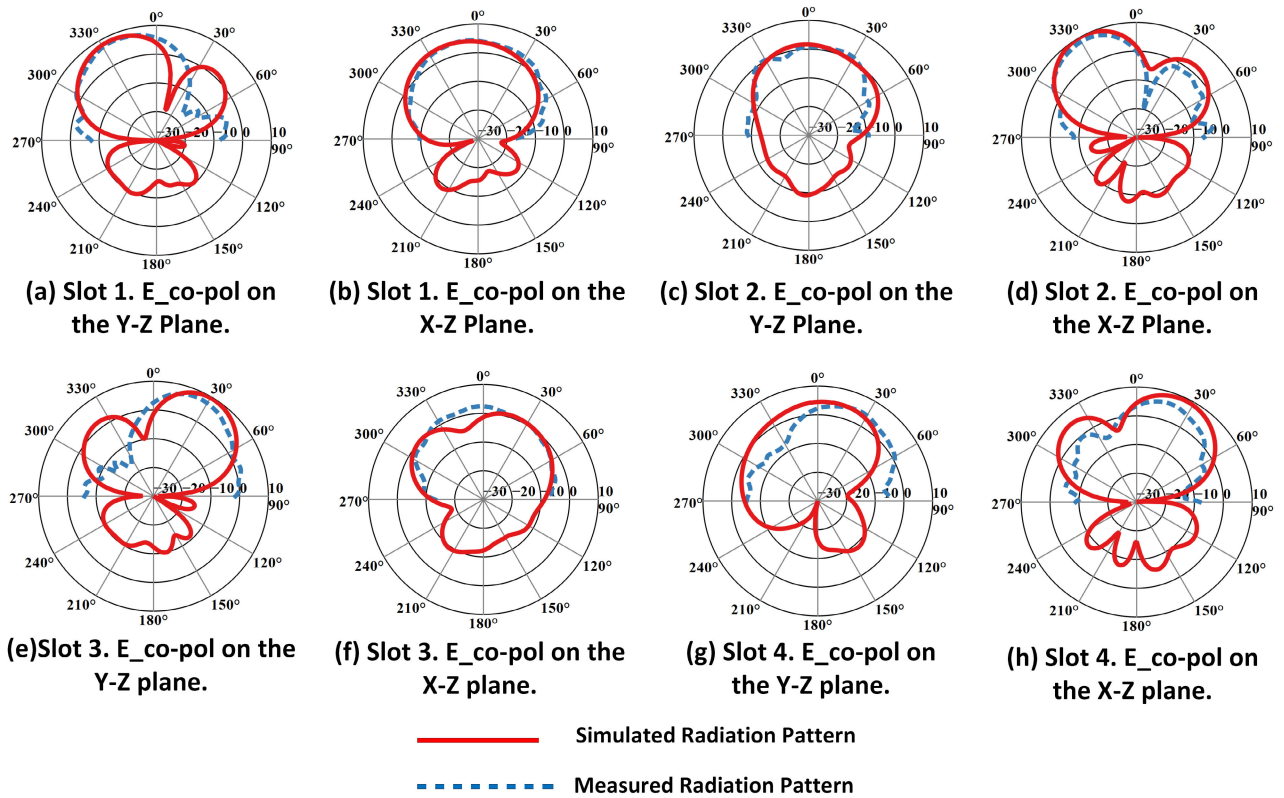- - - Measured Radiation Pattern

FIGURE 10. Simulated and measured radiation patterns of 4 pattern configurations of a single-element antenna.

use of an electric reflector, and $A.F.(planar\ array)$ is the array factor due to the planar array.

After that, a 4 × 4 antenna array is analyzed, as shown in Fig. 12. The radiation patterns for the four configurations are shown in Figs. 13 and 14. The radiation patterns shown in Fig. 13 present the gain on the Y-Z plane for Slot 1 and Slot 3, when the progressive phase in the y-direction is $\beta_y = 110^o$ and $\beta_y = -110^o$, respectively. The radiation patterns shown in Fig. 14 present the gain on the X-Z plane for Slot 2 and Slot 4, when the progressive phase in the x-direction is $\beta_x = 110^o$ and $\beta_x = -140^o$, respectively. It can be seen that Slot 1 configuration achieves a peak gain of 17.4 dBi at $\theta = -30^o$ on the Y-Z plane, HPBW of 20°, and a Side Lobe Level of -10 dB. Slot 2 configuration obtains a peak gain of 16.2 dBi at $\theta = -30^o$ on the X-Z plane, HPBW of 20°, and a Side Lobe Level of -6.2 dB. Slot 3 configuration obtains a peak gain of 17 dBi at $\theta = 30^o$ on the Y-Z plane, HPBW of 20°, and a Side Lobe Level of -8 dB. Slot 4 configuration achieves a peak gain of 13.2 dBi at $\theta = 30^o$ on the X-Z plane, HPBW of 20°, and a Side Lobe Level of -5 dB. The radiation beam can be steered in the range $-50° \leq \theta \leq 50°$ in the planes at $\phi = 0°$ and $\phi = 90°$, without a high gain loss. It is worth mentioning that the best performance is obtained from the reconfigurable antenna array if the suitable slot configuration is chosen for a specific radiation direction in space. For example, if beam steering is required in the

+y direction, D3 diodes should be ON for the sixteen array elements. It can also be seen from Fig. 13 and Fig. 14 that the side-lobe levels are relatively high. This is because the spacings between the array elements are larger than half a wavelength. The cross-polarization level is about -12 dB.

In addition, the Cumulative Distribution Function (CDF) for the coverage efficiencies of the simulated radiation patterns for the 2 × 2 array is obtained using 500 different simulation data sets. The simulated CDF of the coverage efficiencies is shown in Fig. 15. The coverage efficiency when Slot 1 is activated on the four array elements and phase shifts are applied between the four elements to steer the beam is shown in Fig. 15. The coverage efficiencies are also shown for Slot 2, Slot 3, and Slot 4 configurations. The coverage efficiency for the pattern reconfigurable 2 × 2 antenna array, where the array can be operated using Slot 1, Slot 2, Slot 3, or Slot 4 on the four array elements, is also shown in Fig. 15. The pattern reconfigurable antenna array can be operated using Slot 1, Slot 2, Slot 3, or Slot 4 configuration because of the installed 16 PIN diodes. The coverage efficiency increases by 2.65 dB at the 50% threshold, thanks to the pattern reconfigurability of the antenna array. It can be seen from Fig. 15 that 50% of the spherical coverage of the array antenna will have a pattern gain of -1 dB when the pattern reconfigurable antenna array is used.
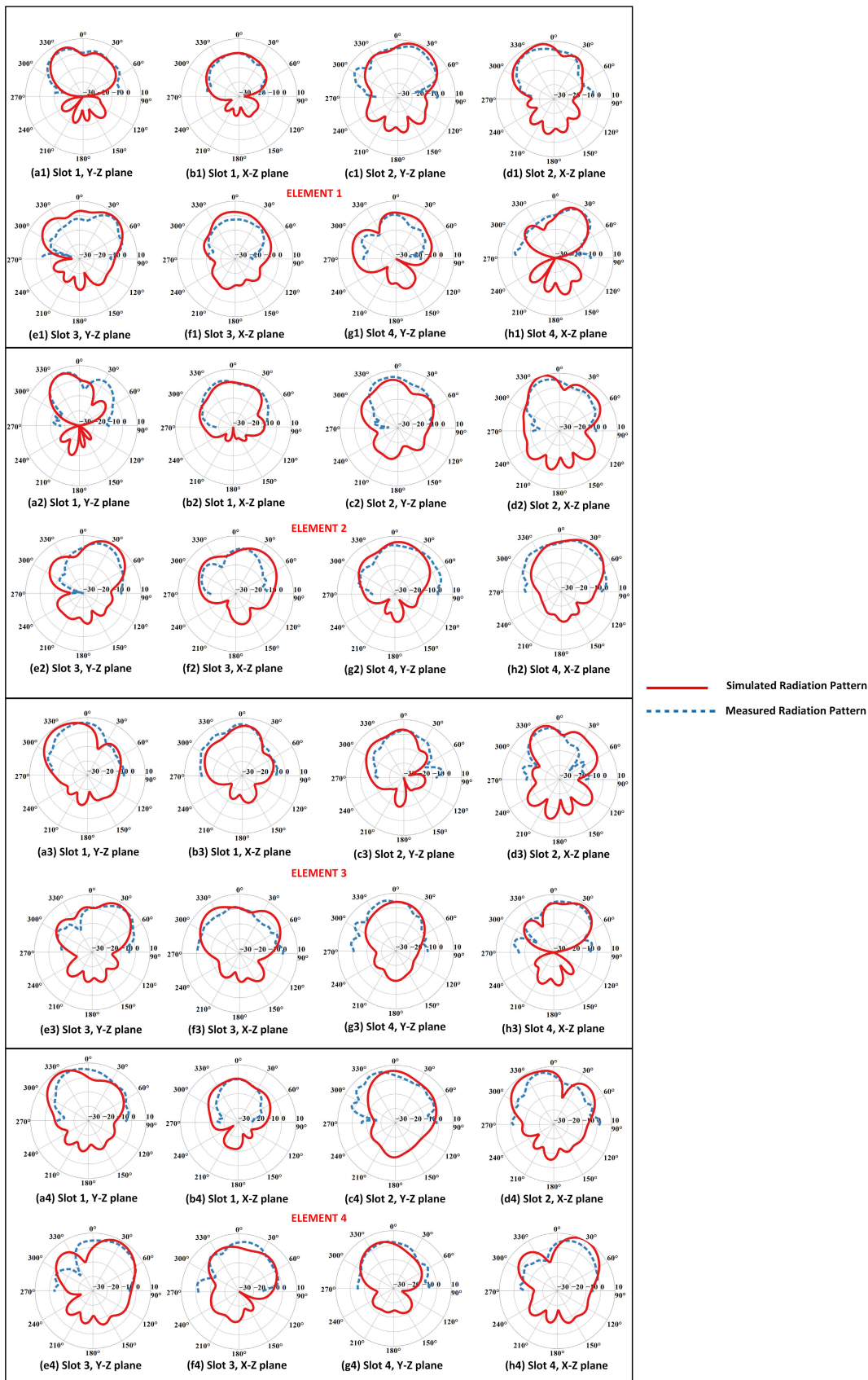
FIGURE 11. Simulated and measured far-field co-polarized radiation patterns for each element in the proposed 2 × 2 antenna array.
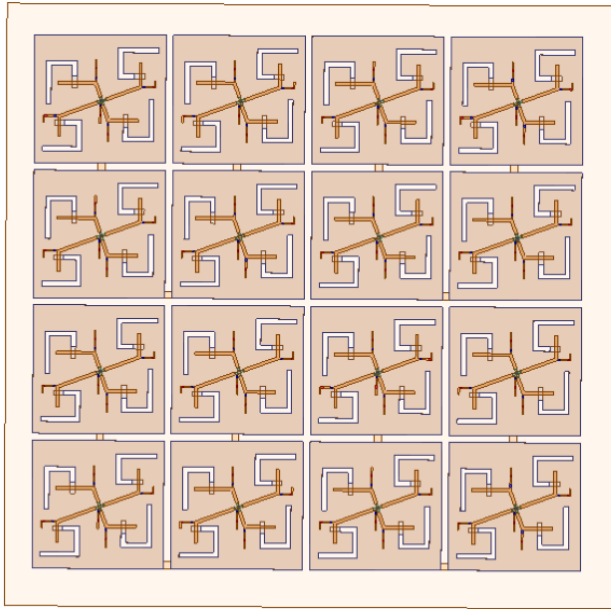
FIGURE 12. The geometry of the proposed pattern reconfigurable 4 × 4 antenna array for the Array Mode operation.
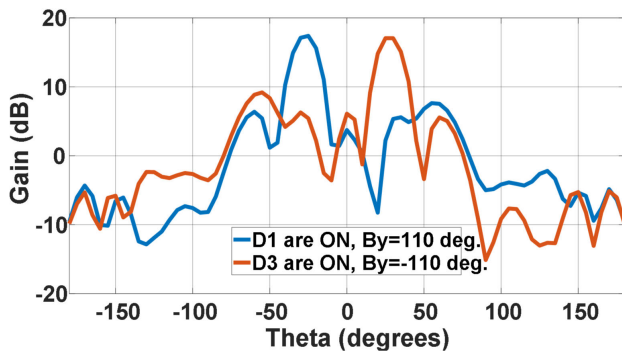

FIGURE 13. Simulated radiation patterns of the Array Mode for Slot 1 and Slot 3 configurations along the Y-Z plane.
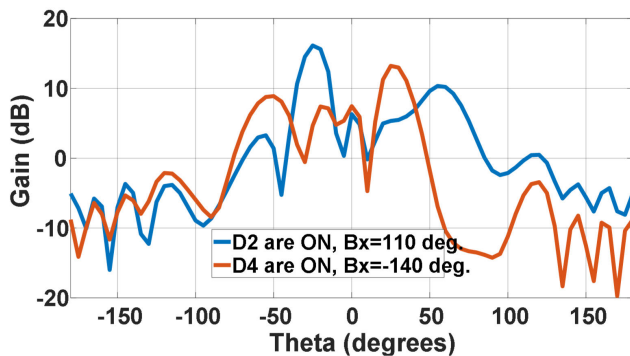

FIGURE 14. Simulated radiation patterns of the Array Mode for Slot 2 and Slot 4 configurations along the X-Z plane.

B. MIMO MODE RESULTS
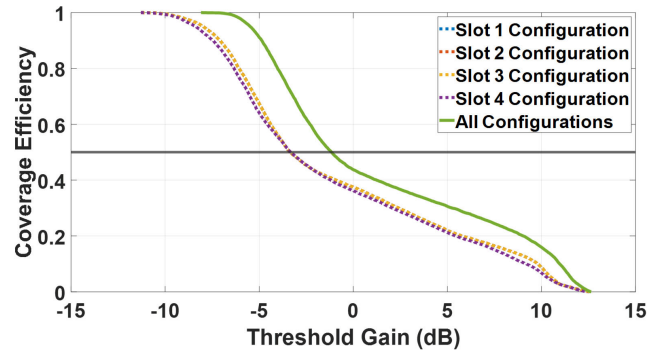In the MIMO Mode, different diodes (D1−D4) are ON in the 4 MIMO elements; e.g., D1 is ON for element 1, D2 is

FIGURE 15. Simulated coverage efficiency of the pattern reconfigurable 2 × 2 antenna array.

TABLE 5. Simulated Radiation Efficiencies of the Radiating Slots in the 2 × 2 MIMO Antenna.

Radiating Slot	Efficiency	Radiating Slot	Efficiency
Element 1, Slot 1	83%	Element 3, Slot 1	77%
Element 1, Slot 2	61%	Element 3, Slot 2	73%
Element 1, Slot 3	77%	Element 3, Slot 3	81%
Element 1, Slot 4	65%	Element 3, Slot 4	72%
Element 2, Slot 1	78%	Element 4, Slot 1	76%
Element 2, Slot 2	70%	Element 4, Slot 2	80%
Element 2, Slot 3	81%	Element 4, Slot 3	82%
Element 2, Slot 4	73.5%	Element 4, Slot 4	71%
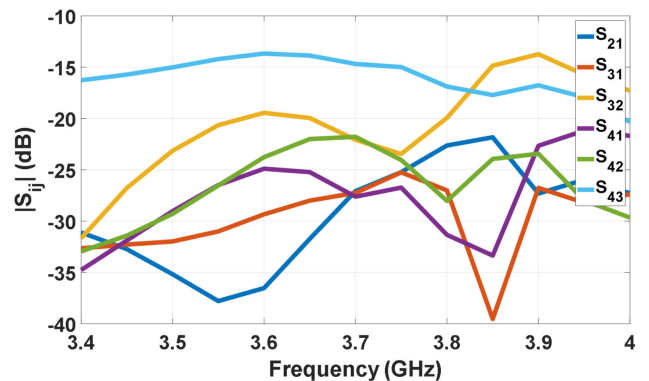
FIGURE 16. Simulated $|S_{ij}|$ between different ports of the MIMO antenna.

ON for element 2, D3 is ON for element 3, and D4 is ON for element 4. Therefore, 16 different combinations can be achieved for the MIMO mode by changing the diode status in the MIMO elements. The Envelope Correlation Coefficients (ECCs) between the proposed MIMO antenna radiation patterns are small because they are oriented in different directions and achieve different linear polarizations. The ECCs between the radiation patterns of the 2 × 2 MIMO antenna are calculated using the field equation [5], [23],

$$\rho_e^{ij} \approx \frac{|\iint e^{-i}(\theta,\phi) \times e^{-j*}(\theta,\phi)\,d\Omega|^2}{\iint |e^{-i}(\theta,\phi)|^2\,d\Omega \times \iint |e^{-j}(\theta,\phi)|^2\,d\Omega}, \quad (23)$$

TABLE 6. Simulated ECCs Between the Radiation Patterns of the Proposed 2 × 2 MIMO Antenna at 3.65 GHz.

Conf.	Slot 1 (E1)	Slot 2 (E2)	Slot 3 (E3)	Slot 4 (E4)	Slot 2 (E1)	Slot 3 (E2)	Slot 4 (E3)	Slot 1 (E4)	Slot 3 (E1)	Slot 4 (E2)	Slot 1 (E3)	Slot 2 (E4)	Slot 4 (E1)	Slot 1 (E2)	Slot 2 (E3)	Slot 3 (E4)
Slot 1 (E1)	1	0.0048	0.001	0.0113	0.1623	0.1194	0.01	0.0337	0.0095	0.0369	0.0005	0.0017	0.0472	0.0017	0.0033	0.0187
Slot 2 (E2)	0.0048	1	0.0027	0.0032	0.0259	0.1321	0.0215	0.0128	0.0014	0.0392	0.0387	0.185	0.0428	0.3646	0.0074	0.00129
Slot 3 (E3)	0.001	0.0027	1	0.0099	0.0229	0.1092	0.4039	0.1188	0.0028	0.0582	0.128	0.0602	0.00129	0.0241	0.0154	0.0155
Slot 4 (E4)	0.0113	0.0032	0.0099	1	0.0408	0.0288	0.0472	0.1028	0.1	0.009	0.0074	0.0593	0.0237	0.0063	0.0478	0.3703
Slot 2 (E1)	0.1623	0.0259	0.0229	0.0408	1	0.0117	0.0224	0.0017	0.0345	0.0288	0.0011	0.0068	0.1432	0.0442	0.0029	0.0093
Slot 3 (E2)	0.1194	0.1321	0.1092	0.0288	0.0117	1	0.0363	0.0474	0.0591	0.1531	0.0912	0.0483	0.0704	0.0455	0.0228	0.0526
Slot 4 (E3)	0.01	0.0215	0.4039	0.0472	0.0224	0.0363	1	0.0528	0.0001	0.072	0.2017	0.0941	0.0053	0.0077	0.0073	0.0696
Slot 1 (E4)	0.0337	0.0128	0.1188	0.1028	0.0017	0.0474	0.0528	1	0.0577	0.0345	0.0075	0.1282	0.0218	0.026	0.0127	0.0583
Slot 3 (E1)	0.0095	0.0014	0.0028	0.1	0.0345	0.0591	0.0001	0.0577	1	0.0008	0.0051	0.0019	0.1278	0.0041	0.015	0.166
Slot 4 (E2)	0.0369	0.0392	0.0582	0.009	0.0288	0.1531	0.072	0.0345	0.0008	1	0.0086	0.0003	0.0331	0.0221	0.0022	0.0123
Slot 1 (E3)	0.0005	0.0387	0.128	0.0074	0.0011	0.0912	0.2017	0.0075	0.0051	0.0086	1	0.0294	0.0182	0.0832	0.1379	0.0015
Slot 2 (E4)	0.0017	0.185	0.0602	0.0593	0.0068	0.0483	0.0941	0.1282	0.0019	0.0003	0.0294	1	0.0033	0.0076	0.0346	0.012
Slot 4 (E1)	0.0472	0.0428	0.00129	0.0237	0.1432	0.0704	0.0053	0.0218	0.1278	0.0331	0.0182	0.0033	1	0.0014	0.0068	0.0129
Slot 1 (E2)	0.0017	0.3646	0.0241	0.0063	0.0442	0.0455	0.0077	0.026	0.0041	0.0221	0.0832	0.0076	0.0014	1	0.0016	0.0001
Slot 2 (E3)	0.0033	0.0074	0.0154	0.0478	0.0029	0.0228	0.0073	0.0127	0.015	0.0022	0.1379	0.0346	0.0068	0.0016	1	0.00129
Slot 3 (E4)	0.0187	0.00129	0.0155	0.3703	0.0093	0.0526	0.0696	0.0583	0.166	0.0123	0.0015	0.012	0.0129	0.0001	0.00129	1

TABLE 7. Comparison Table Between the Proposed Antenna with Some Base-Station Antennas in the Literature.

Ref.	f_r (GHz)	B.W. (MHz)	Max. ECC	Size (mm)	Gain	Modes	Isolation	Eff.	# Ports	Design Method	Complexity	# MIMO states	FOM
[12]	2.45	200	0.5	120 × 60	-	MIMO	20 dB	60%	2	Characteristic modes	low (4 diodes)	3	1.47
[14]	3.6, 5.5	200, 775	0.016	82.4 × 82.4	4.6 dBi	MIMO	19.6 dB	80%	4	Orthogonal Orientation	High (Filling Water to Cavity)	8	0.342
[15]	5.9	-	-	153 × 25.4	-	MIMO	-	-	2	tuning metamaterial	High (100 diodes)	-	-
[16]	2.65	96	0.05	50 × 70	3 dBi	MIMO	15 dB	80%	2	Different radiators	Medium (6 diodes)	4	0.1156
[17]	2.45	260	0.011 (S-equation)	102 × 80	4.7 dBi	MIMO	16.5 dB	82.5%	2	Yagi Uda	Low (8 diodes)	9	2.33
[19]	3.5	50	-	400 × 270	6.86 dBi	MIMO	15 dB	70%	1	Array Factor	high (64 diodes)	40	0.65
This work	3.65	200	0.1194	140 × 140	9 dBi & 12.5 dBi (simulated)	MIMO & Array	20 dB	80% (simulated)	4	Yagi Uda	Medium (16 diodes)	16	5.57

(a) Element 1: D1 is ON. Element 2: D2 is ON. Element 3: D3 is ON. Element 4: D4 is ON.

(b) Element 1: D2 is ON. Element 2: D3 is ON. Element 3: D4 is ON. Element 4: D1 is ON.

(c) Element 1: D3 is ON. Element 2: D4 is ON. Element 3: D1 is ON. Element 4: D2 is ON.

(d) Element 1: D4 is ON. Element 2: D1 is ON. Element 3: D2 is ON. Element 4: D3 is ON.
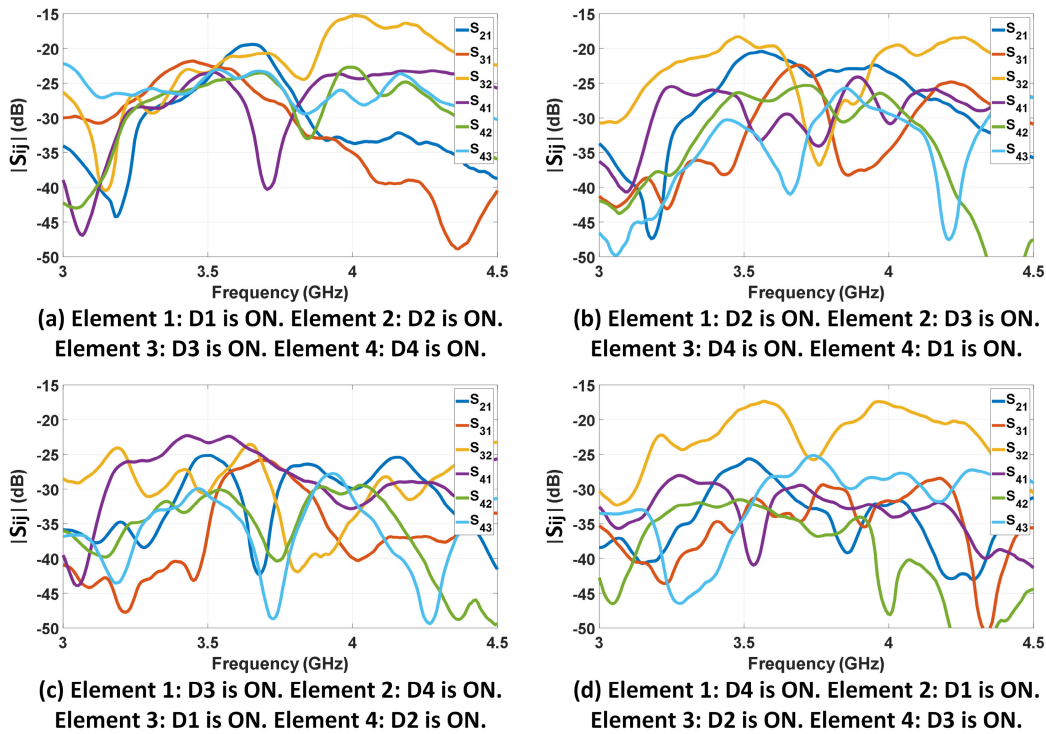
FIGURE 17. Measured $|S_{ij}|$ between ports of the MIMO antenna for different MIMO combinations.
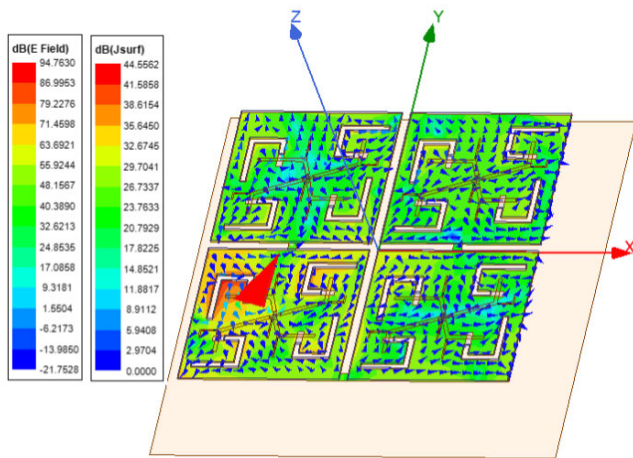

FIGURE 18. Electric field and vector current distribution on the antenna array when Port 2 is excited, and Slot 1 on Element 2 is activated.

where $d\Omega = sin\theta d\theta d\phi$, $e^{-i}(\theta, \phi)$ is the radiated far-field electric field for the ith configuration, and the asterisk indicates the complex conjugate. The simulated ECCs between the radiation patterns of the 16 pattern configurations of the 2×2 MIMO antenna at 3.65 GHz are shown in Table 6, where it can be seen that the maximum ECC in the bandwidth of operation is 0.1194 when the activated slots are in different antenna elements. The ECCs are below 0.18 within the bandwidth of interest, even between the radiation patterns of the slots on the same element. The measured ECCs are

expected to be in reasonable agreement with the simulated ECCs since the measured and simulated radiation patterns are in a good agreement. It is worth mentioning that the ECCs are calculated with the assumption that the environment is isotropic, and the incoming signals are sinusoidal. In addition, it can be seen from Table 6 that if the MIMO antenna is designed with 16 ports feeding each slot, then the channel capacity is going to increase by a factor of 16 as shown in Eq. (24) assuming a full-rank MIMO channel [22].

$$C = N \times log_2 \left(1 + \frac{SNR}{N}\right), \qquad (24)$$

where C is the channel capacity, N is the number of elements on the transmitting and receiving MIMO antennas, and SNR is the Signal-to-Noise ratio.

The simulated $|S_{ij}|$ between the 4 MIMO ports is shown in Fig. 16. The measured $|S_{ij}|$ between the four ports of the MIMO antenna for four different combinations is shown in Fig. 17. It can be seen in Fig. 17 that the isolation in the bandwidth of operation between the 4 MIMO ports is always more than 20 dB. The high isolation between the MIMO ports is achieved because of the defective ground structure (the rectangular slots in the ground plane). In addition, the U-slots are oriented orthogonal to each other to provide orthogonal linear polarization, and to enhance the isolation. The isolation between ports 2 and 3, when Slot 1 is ON in element 2, and Slot 2 is ON in element 3, as shown in Fig. 17(d), is less than 20 dB. This is because the dominant current on Slot 1 of Element 2 is +y-directed towards the ground of Element

3, which increases the current coupling between ports of the two elements, as shown in Fig. 18. In addition, the ground of Element 3 is positioned on the direction of the radiation pattern of Slot 1 on Element 2; as a result, the electric field is more coupled to the ground of Element 3. On the other hand, the simulated radiation efficiencies for each radiating slot in the 2 × 2 MIMO antenna are shown in Table 5, where it can be seen that the efficiencies of the slots in the MIMO array are different from the efficiencies of the corresponding slots in the single-element antenna due to higher mutual couplings between slots and ports in the MIMO array. However, the difference between the radiation efficiencies of the slots in the MIMO array and the single-element antenna is reasonable, showing a good isolation between the radiating slots and low mutual coupling effects in the MIMO antenna.

V. DISCUSSIONS AND CONCLUSION

The 2 × 2 antenna array is a good candidate for small-cell base-stations. Thanks to its pattern and polarization reconfigurability, two functional modes are achieved. In the Array Mode, higher gain and broader steering capabilities are achieved. In the MIMO Mode, many combinations and enhanced channel capacity are realized.

The proposed pattern reconfigurable 2 × 2 antenna array is compared in Table 7 with the previous pattern reconfigurable MIMO antennas shown in [12], [13], [14], [15], [16], [17], [18], and [19]. The proposed pattern reconfigurable slot-based 2 × 2 antenna in this article allows two functional modes, Array and MIMO modes. The peak gain for a single radiating slot is 9 dBi, with a radiation efficiency of 80%, exceeding the achieved gains in [9], [10], and [11]. The Array Mode can further enhance the peak gain to 17.4 dBi for more wireless coverage. The MIMO mode enables multiple combinations with minimum isolation of 20 dB and a maximum ECC of 0.1194 in the bandwidth of interest, showing a better performance than previous antenna designs. The proposed antenna array is relatively compact. The achieved operation bandwidth for the proposed design competes with the previously published designs. The following Figure of Merit (FOM) equation shown in Eq. (25) compares the proposed antenna array with the proposed antennas in table 7.

$$FOM = \frac{Gain \times \#States \times Efficiency \times BW \times \#Modes}{Complexity}, \quad (25)$$

where *Gain* is the antenna gain in linear scale, *#States* is the number of pattern MIMO states, *Efficiency* is the percentage efficiency of the antenna, *BW* is the percentage bandwidth, *#Modes* is the number of functional modes of the antenna, and the *Complexity* is the complexity of the pattern reconfigurable MIMO antenna design, with a scale from 1 to 3, where 1 is for Low complexity, 2 is for Medium complexity, and 3 is for High complexity. It can be seen from Table 7 that the antenna of this work achieves the best FOM.

In conclusion, the paper has presented a new pattern reconfigurable 2 × 2 elements. The antenna has a MIMO Mode and Array Mode with good performance. The used single-element antenna was a pattern reconfigurable U-slot with four uncorrelated pattern configurations, with an average efficiency of 80%, a peak gain of 9.35 dBi, and an overlapped measured −10 dB impedance bandwidth of 200 MHz around 3.65 GHz resonant frequency. The MIMO Mode exhibits good performance at 3.65 GHz with a maximum ECC of 0.1194 between the 16 configurations and a minimum isolation of 20 dB. The Array Mode of the antenna shows good performance at 3.65 GHz with a peak gain reaching 17.4 dBi, −12 dB cross-polarization, and a 50% coverage efficiency with a gain of −1 dB. The antenna is with compact size and suitable for small-cell base-station applications.

REFERENCES

[1] (2019). *Cisco Visual Networking Index: Global Mobile Data Traffic Forecast Update 2017-2022 White Paper*. Cisco. [Online]. Available: https://www.cisco.com/c/en/us/solutions/collateral/service-provider/visual-networking-index-vni/white-paper-c11-738429.html

[2] F. Hu, *Opportunities in 5G Networks: A Research and Development Perspective*. Boca Raton, FL, USA: CRC Press, 2016.

[3] S.-H. Chen, J.-S. Row, and K.-L. Wong, "Reconfigurable square-ring patch antenna with pattern diversity," *IEEE Trans. Antennas Propag.*, vol. 55, no. 2, pp. 472–475, Feb. 2007.

[4] Z. Lu, X. Yang, and G. Tan, "A multidirectional pattern-reconfigurable patch antenna with CSRR on the ground," *IEEE Antennas Wireless Propag. Lett.*, vol. 16, pp. 416–419, 2017.

[5] M.-I. Lai, T.-Y. Wu, J.-C. Hsieh, C.-H. Wang, and S.-K. Jeng, "Compact switched-beam antenna employing a four-element slot antenna array for digital home applications," *IEEE Trans. Antennas Propag.*, vol. 56, no. 9, pp. 2929–2936, Sep. 2008.

[6] Z. Lu, X. Yang, and G. Tan, "A wideband printed tapered-slot antenna with pattern reconfigurability," *IEEE Antennas Wireless Propag. Lett.*, vol. 13, pp. 1613–1616, 2014.

[7] S. V. S. Nair and M. J. Ammann, "Reconfigurable antenna with elevation and azimuth beam switching," *IEEE Antennas Wireless Propag. Lett.*, vol. 9, pp. 367–370, 2010.

[8] Y. F. Cao and X. Y. Zhang, "A wideband beam-steerable slot antenna using artificial magnetic conductors with simple structure," *IEEE Trans. Antennas Propag.*, vol. 66, no. 4, pp. 1685–1694, Apr. 2018.

[9] S.-W. Su, "High-gain dual-loop antennas for MIMO access points in the 2.4/5.2/5.8 GHz bands," *IEEE Trans. Antennas Propag.*, vol. 58, no. 7, pp. 2412–2419, Jul. 2010.

[10] W. Han, X. Zhou, J. Ouyang, Y. Li, R. Long, and F. Yang, "A six-port MIMO antenna system with high isolation for 5-GHz WLAN access points," *IEEE Antennas Wireless Propag. Lett.*, vol. 13, pp. 880–883, 2014.

[11] Y. Pan, Y. Cui, and R. Li, "Investigation of a triple-band multibeam MIMO antenna for wireless access points," *IEEE Trans. Antennas Propag.*, vol. 64, no. 4, pp. 1234–1241, Apr. 2016.

[12] K. Li and Y. Shi, "A pattern reconfigurable MIMO antenna design using characteristic modes," *IEEE Access*, vol. 6, pp. 43526–43534, 2018.

[13] M. Hasan, I. Bahçeci, and B. A. Cetiner, "Downlink multi-user MIMO transmission for radiation pattern reconfigurable antenna systems," *IEEE Trans. Wireless Commun.*, vol. 17, no. 10, pp. 6448–6463, Oct. 2018.

[14] A. Singh and C. E. Saavedra, "Fluidically reconfigurable MIMO antenna with pattern diversity for sub-6-GHz 5G relay node applications," *Can. J. Electr. Comput. Eng.*, vol. 43, no. 2, pp. 92–99, Spring. 2020.

[15] I. Yoo, M. F. Imani, T. Sleasman, H. D. Pfister, and D. R. Smith, "Enhancing capacity of spatial multiplexing systems using reconfigurable cavity-backed metasurface antennas in clustered MIMO channels," *IEEE Trans. Commun.*, vol. 67, no. 2, pp. 1070–1084, Feb. 2019.

[16] H. Li, B. K. Lau, and S. He, "Design of closely packed pattern reconfigurable antenna array for MIMO terminals," *IEEE Trans. Antennas Propag.*, vol. 65, no. 9, pp. 4891–4896, Sep. 2017.

[17] L. Han, Y. Ping, Y. Liu, G. Han, and W. Zhang, "A low-profile pattern reconfigurable MIMO antenna," *IEEE Access*, vol. 8, pp. 34500–34506, 2020.

[18] J. Kowalewski, J. Mayer, T. Mahler, and T. Zwick, "Evaluation of a wideband pattern-reconfigurable multiple antenna system for vehicular applications," in *Proc. 12th Eur. Conf. Antennas Propag. (EuCAP)*, Apr. 2018, pp. 1–5.

[19] X. G. Zhang, W. X. Jiang, H. W. Tian, Z. X. Wang, Q. Wang, and T. J. Cui, "Pattern-reconfigurable planar array antenna characterized by digital coding method," *IEEE Trans. Antennas Propag.*, vol. 68, no. 2, pp. 1170–1175, Feb. 2020.

[20] Y. Tawk, J. Constantine, and C. G. Christodoulou, "An eight-element reconfigurable diversity dipole system," *IEEE Trans. Antennas Propag.*, vol. 66, no. 2, pp. 572–581, Feb. 2018.

[21] C. A. Balanis, *Antenna Theory: Analysis and Design*. New York, NY, USA: Wiley, 1997.

[22] M. U. Khan, W. A. A. Al-Saud, and M. S. Sharawi, "Channel capacity measurement of a 4-element printed MIMO antenna system," in *Proc. German Microw. Conf. (GeMiC)*, Mar. 2014, pp. 1–4.

[23] M. S. Sharawi, "Printed multi-band MIMO antenna systems and their performance metrics [wireless corner]," *IEEE Antennas Propag. Mag.*, vol. 55, no. 5, pp. 218–232, Oct. 2013.

SAEED HAYDHAH (Student Member, IEEE) received the M.Sc. degree from the King Fahd University of Petroleum and Minerals (KFUPM), Dhahran, Saudi Arabia. He is currently pursuing the Ph.D. degree in antennas/radio frequency engineering with the Electrical and Computer Department, Concordia University, Montreal, QC, Canada. From 2019 to 2020, he was a Visiting Student with the Laboratory of Electronics, Antennas and Telecommunications (LEAT), Université Côte d'Azur, Sophia Antipolis, France. During the M.Sc. degree, he was a member of the Antennas and Microwave Structure Design Laboratory (AMSDL), KFUPM. His current research interests include the design of 5G photonic integrated mmWave antennas, mmWave filtering antenna design, and the IoT antenna design.

RYAN GOLD is currently pursuing the B.Eng. degree in electrical engineering with the Electrical and Computer Engineering Department, Concordia University, Montreal, QC, Canada. He joins the Photonic and Antenna Laboratories, Concordia University, to collaborate on the design of a mmWave photonic integrated antenna and 5G mmWave filtering antenna design.

ZHIYONG DONG received the B.S. and M.S. degrees in electrical and electronics engineering from the Beijing Institute of Technology, Beijing, China, in 2016 and 2019, respectively. He is currently pursuing the Ph.D. degree in electrical engineering with Concordia University, Montreal, Canada. His current research interests include radiofrequency design, especially amplifier-integrated antennae and packaged transmission lines.

FABIEN FERRERO (Member, IEEE) received the Ph.D. degree in electrical engineering from the University of Nice-Sophia Antipolis, in 2007. From 2008 to 2009, he was with IMRA Europe (Aisin Seiki Research Center) as a Research Engineer and developed automotive antennas. In 2010, he was an Associate Professor with the Polytechnic School, Université Nice Sophia Antipolis. Since 2018, he has been a Full Professor with Université Côte d'Azur. He is currently a member of Laboratoire d'Electronique, Antennes et Telecommunications (LEAT). His current research interests include the design and measurement of millimetric antennas, the IoT systems, and reconfigurable antennas.

LEONARDO LIZZI (Senior Member, IEEE) received the M.Sc. degree in telecommunication engineering and the Ph.D. degree in information and communication technology from the University of Trento, Italy, in 2007 and 2011, respectively. During the Ph.D. degree, he has been a Visiting Researcher with The Pennsylvania State University, USA, and the University of Nagasaki, Japan. From 2011 to 2014, he was a Postdoctoral Researcher with the Laboratory of Electronics, Antennas and Telecommunications (LEAT), Université Côte d'Azur, Sophia Antipolis, France. Since 2014, he has been a Maître de Conférences (an Associate Professor) with Université Côte d'Azur. His current research interests include reconfigurable, miniature, multi-standards antennas for the Internet of Things applications, wearable devices, and 5G terminals.

MOHAMMAD S. SHARAWI (Senior Member, IEEE) was with the King Fahd University of Petroleum and Minerals (KFUPM), Saudi Arabia, from 2009 to 2018. He founded and directed the Antennas and Microwave Structure Design Laboratory (AMSDL), KFUPM. He was a Visiting Professor with the Intelligent Radio (iRadio) Laboratory, Electrical Engineering Department, University of Calgary, Alberta, Canada, in Summer–Fall 2014. He was a Visiting Research Professor with Oakland University, in Summer 2013. He is currently a Professor of electrical engineering with Polytechnique Montréal, Montréal, QC, Canada. He is also a member of the Poly-Grames Research Center, Polytechnique Montréal. He has published more than 380 papers in refereed journals and international conferences, ten book chapters, one single-authored book titled *Printed MIMO Antenna Engineering* (Artech House, 2014), and the lead author of the recent book *Design and Applications of Active Integrated Antennas* (Artech House, 2018). He has 28 issued and 12 pending patents in the U.S. patent office. His current research interests include multiband printed multiple-input-multiple-output (MIMO) antenna systems, reconfigurable and active integrated antennas, applied electromagnetics, millimeter-wave MIMO antennas, and integrated 4G/5G antennas for wireless handsets and access points.

He served on the technical and organizational program committees for several international conferences, such as EuCAP, APS, IMWS-5G, APCAP, iWAT, and many others. He is serving as an Associate Editor for the IEEE ANTENNAS AND WIRELESS PROPAGATION LETTERS (AWPL) and *IET Microwaves, Antennas and Propagation* (MAP) and an Area Editor for *Microwave and Optical Technology Letters* (MOP) (Wiley). He is the specialty Editor of the newly launched *Frontiers in Communications and Networking*, the System and Test-Bed Design Section. He is IEEE Distinguished Lecturer for the Antennas and Propagation Society from 2023–2025.

AHMED A. KISHK (Life Fellow, IEEE) has been a Professor with Concordia University, Montréal, QC, Canada, since 2011, and the Tier 1 Canada Research Chair of Advanced Antenna Systems. He has published more than 430 refereed journal articles and 520 international conference papers, and 125 local and regional conference papers. He has coauthored four books and several chapters and was the editor of six books. He offered several short courses at international conferences. His current research interest includes electromagnetic applications. He has recently worked on millimeter-wave antennas for 5G/6G applications, analog beamforming networks, electromagnetic bandgap, phased array antennas, reflectors/transmit arrays, and wearable antennas. In addition, he is a pioneer in dielectric resonator antennas, microstrip antennas, small antennas, microwave sensors, multi-function antennas, microwave circuits, and feeds for parabolic reflectors.

He was a member of the AP-S AdCom, from 2013 to 2015, and the 2017 AP-S President. He is a member of several IEEE societies, such as the Antennas and Propagation Society, Microwave Theory and Techniques, Electromagnetic Compatability, Communications, Vehicular Technology Society, and Signal Processing. He is a Senior Member of the International Union of Radio Science Commission B. In recognition, for contributions and continuous improvements to teaching and research to prepare students for future careers in antennas and microwave circuits, a fellow of the Electromagnetic Academy and the Applied Computational Electromagnetics Society (ACES). He and his students received several awards. He won the 1995 and 2006 outstanding paper awards for papers published in the *Applied Computational Electromagnetic Society Journal*. He received the 1997 Outstanding Engineering Educator Award from the Memphis Section of the IEEE. He received the Outstanding Engineering Faculty Member, in 1998 and 2009, and the Faculty Research Award for Outstanding Research Performance, in 2001 and 2005. He received the Award of Distinguished Technical Communication for *IEEE Antennas and Propagation Magazine*'s Entry, in 2001. He also received the Valued Contribution Award for an Outstanding Invited Presentation, "EM Modeling of Surfaces with STOP or GO Characteristics—Artificial Magnetic Conductors and Soft and Hard Surfaces," from the Applied Computational Electromagnetic Society. He received the Microwave Theory and Techniques Society Microwave Prize, in 2004. He received the 2013 Chen-To-Tai Distinguished Educator Award from the IEEE Antennas and Propagation Society. He was a Distinguished Lecturer of the Antennas and Propagation Society, from 2013 to 2015. He was an Editor of *Antennas and Propagation Magazine*, from 1993 to 2014, and the Editor-in-Chief of the *Applied Computational Electromagnetic Society Journal*, from 1998 to 2001.

● ● ●